Second-Order Phase Transition At The Phase Boundary Through The FeRh First-Order Metamagnetic Phase Transition

Jamie R. Massey,[1,*] Rowan C. Temple,[1] Trevor P. Almeida,[2] Ray Lamb,[2] Nicolas A. Peters,[1,3] Richard P. Campion,[4] Raymond Fan,[5] Damien McGrouther,[2] Stephen McVitie,[2] Paul Steadman,[5] and Christopher H. Marrows[1,†]

[1] *School of Physics and Astronomy, University of Leeds, Leeds LS2 9JT, United Kingdom.*
[2] *SUPA, School of Physics and Astronomy, University of Glasgow, Glasgow, G12 8QQ, United Kingdom.*
[3] *School of Electronic and Electrical Engineering, University of Leeds, Leeds, LS2 9JT, United Kingdom.*
[4] *School of Physics and Astronomy, University of Nottingham, Nottingham, NG7 2RD, United Kingdom.*
[5] *Diamond Light Source, Chilton, Didcot, OX11 0DE, United Kingdom.*

(Dated: December 19, 2019)

The phase coexistence present through first-order phase transitions implies the presence of phase boundary walls, which can be of finite size. Better understanding of the phase boundary wall properties will provide an insight into the dynamics of first-order phase transitions. Here, by combining x-ray photon correlation spectroscopy investigations with magnetometry measurements of magnetic relaxation through the thermally activated first-order metamagnetic phase transition present in the B2-ordered FeRh alloy, we are able to isolate the dynamic behaviour of the phase boundary wall present in this system. These investigations reveal a change in the nature of the dynamic behaviour and critical scaling of the relaxation time centred around the point of maximum phase coexistence within the phase transition. All of this behaviour can be attributed to the introduction of exchange coupling across the phase boundary wall and raises questions about the role of latent heat in dynamic behaviour of this region.

B2-ordered FeRh undergoes a magnetostructural first-order phase transition (FOPT) from an antiferromagnet (AF) to a ferromagnet (FM) when heated through a transition temperature that is $T_T \sim 380$ K in bulk [1–4]. The coupled nature of the magnetic, electronic and structural aspects of the phase transition, and the fact that it occurs at a technologically relevant temperature make it a material of interest for use in a plethora of proposed data storage and memory architectures [5–11].

The kinetics of the FOPT in FeRh have been studied extensively using a variety of magnetic imaging techniques, most of which focus on the development of the FM regions through the transition [12–20]. The behaviour of the phase boundary wall between the coexisting FM and AF phases through the transition is yet to be studied and is said to play a key - but unknown - role in dynamics of the FOPT [12]. In order to try and investigate the role of the phase boundary wall in the kinetics of the FOPT in FeRh we have performed measurements of the dynamic behaviour of the system throughout the transition using X-Ray Photon Correlation Spectroscopy (XPCS).

XPCS follows the temporal correlations of fine structure present in diffraction features, known as speckle. This technique has been used to characterize the dynamic behaviour of various magnetic systems [21–26]. As the FM domains through the FOPT in FeRh are $\sim$ μm in size, any XPCS investigation must utilize Small Angle X-Ray Scattering (SAXS) [17, 20]. It is possible to enhance the signal from SAXS using resonant magnetic x-ray scattering associated with both x-ray magnetic circular and linear dichroism (XMCD & XMLD) in a process known as Resonant Magnetic SAXS (RMSAXS) [27–29]. Whilst XMCD is sensitive to FM order, XMLD is sensitive to the orientation of the spin-axis of the material and can access both FM and AF order [30]. Here, by combining RMSAXS with both XMCD and XMLD, we were able to probe the dynamic behaviour of both the FM and AF phase fractions through the FOPT. These investigations reveal a change in the nature of the dynamic behaviour, and evidence of critical scaling of the relaxation time, centred on the point of maximum phase coexistence. By comparing this to macroscale measurements of the magnetic relaxation performed using a magnetometer, we are able to attribute the observed behaviour to the influence of exchange coupling upon the phase boundary wall through the FOPT.

Our experiments were performed on a 100 nm thick FeRh film, grown on a GaAs heterostructure substrate with a NiAl buffer layer and then detached and captured between Cu TEM grids for soft x-ray transmission measurements. A laboratory x-ray diffraction (XRD) spectrum acquired for the as-grown film is shown in Fig. 1(a). The observation of the (001) and (002) reflections for both the NiAl and FeRh layers indicates the presence of B2 chemical order. The magnetic transition in the as-grown sample is shown by the black line in Fig. 1(b), where the metamagnetic transition expected for this material system is clearly evident. The transition temperature of FeRh is sensitive to the application of external field [12]. Therefore, for comparison with the XPCS measurements, which are performed without an external field

* J.R.Massey@leeds.ac.uk
† c.h.marrows@leeds.ac.uk

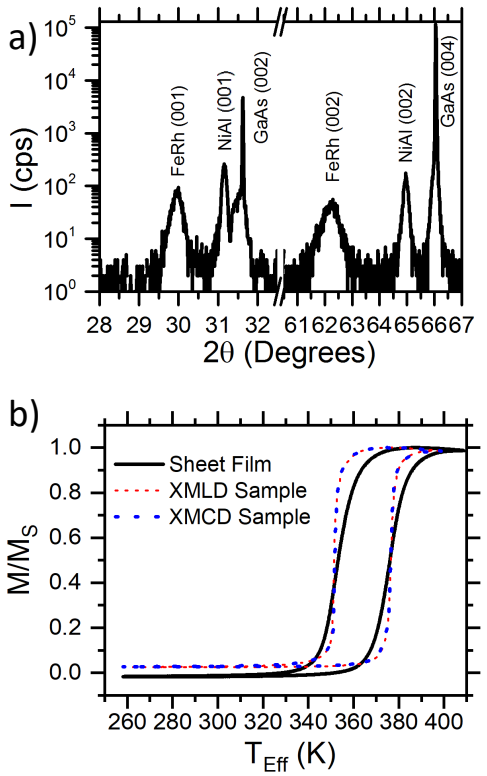

FIG. 1. FeRh thin film sample characterization. (a) XRD scan with indexed Bragg peaks. The presence of both the (001) and (002) reflections for both NiAl and FeRh indicates the presence of B2 chemical order in both layers. (b) Magnetometry traces plotted against T_{Eff} through the range of the transition taken with a 1 T field applied in the film plane. The black line shows the behaviour of the as-grown sample whilst still attached to the substrate, whilst the red and blue lines show the sample behaviour after being made into a membrane. These two lines show samples that were used in the XMLD and XMCD experiments, respectively, which are close to indistinguishable.

applied, this figure is plotted against the effective temperature, T_{Eff}, which is the temperature at which the same magnetization is expected to be achieved in the absence of external field (see supplementary material for calculation) [12, 31].

After undergoing the etching process to be made into a soft x-ray transparent membrane, described in the Methods section, the phase transition was measured again, shown in Fig. 1(b). The magnetic transition is still present and has become considerably sharper. The difference in the magnetic transition between the as-grown and etched states is attributed to the removal of substrate strain. There are two membrane samples here, one used for the XMCD experiments and one used for the XMLD experiments. The two come from the same parent film and have indistinguishable metamagnetic transitions, as seen in Fig. 1(b).

To study the temporal correlations in the system a series of images were acquired at fixed time intervals with alternating polarisation states (see Methods section). Differences between subsequent images with opposite circular helicities or linear polarisation states are referred to as XMCD or XMLD images, respectively. An example of one of these images taken using XMCD after cooling to 390 K is shown in Fig. 2(a), where the presence of a SAXS ring containing speckle is evident. The demonstration of RMSAXS is shown in the supplementary material. The presence of speckle indicates a disordered magnetic structure, as consistent with the magnetic domain state expected in this region of the transition.

Selected images taken through the measurement time for the XMCD measurement performed after cooling to 390 K are shown in Fig. 2(b)-(f). The changing speckle pattern is indicative of a varying magnetic state through the measurement time. To quantify the extent of these changes the temporal auto-correlations for each image series performed at a given temperature are calculated using a g_2 function (see Methods section). Example g_2 functions calculated for various points on the cooling branch measured using XMCD can be seen in Fig. 2(g).

To extract the dynamic behaviour, the g_2 function is fitted by a stretched exponential model written as

$$g_2(\tau) = 1 + A\cos(\omega\tau)e^{-\left(\frac{\tau}{\lambda}\right)^{\beta}}, \qquad (1)$$

where A is the speckle intensity or correlation amplitude, β is the stretching exponent and λ is the relaxation time. This form of the fitting function requires the presence of a static reference signal, for which ω demonstrates the mixing frequency between the dynamic and static signals [22, 32]. The static reference signal measured here originates from the resonant charge scattering in the sample also present at the Fe L_3 edge. Examples of fitting this equation to the g_2 behaviours can be seen by the solid lines in Fig. 2(g). The dynamic behaviour of the system is captured by the β and λ parameters, so that is where our discussion shall now focus.

For investigations using XMCD, it can be seen from Fig. 3(a) that $\beta \approx 1.5$ for temperatures in excess of the transition midpoint on each branch when measured using magnetometry, T_{M}, shown by the dashed lines in Fig. 3. Approaching T_{M}, the value of β is seen to decrease towards 1 when cooling, and rise from that value when heating. The parameter β is used to describe the type of dynamic behaviour seen in the system [26, 33, 34]. When $0 < \beta \leq 1$ the dynamics are diffusive, whilst systems where $1 < \beta \leq 2$ have collective dynamics [23, 26, 33–36]. Systems in which $\beta = 1.5$ present a special case of collective dynamics in which the system is in a 'jammed' state, meaning that relaxation events are unable to propagate through the system [26, 36]. The change in β from 1 to 1.5 for $T \sim T_{\mathrm{M}}$ implies the system sees a change from diffusive to jammed dynamics at this temperature.

The isothermal temporal evolution of FeRhs FOPT has previously been described using the 'droplet' model [37], which is used to model systems where one phase forms

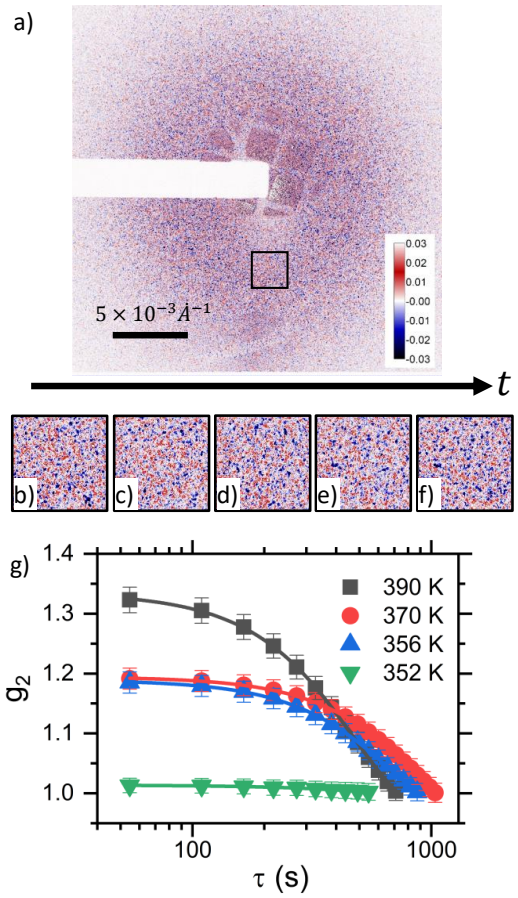

FIG. 2. Transmission RMSAXS patterns and temporal correlation analysis. (a) Image taken on the Fe L_3 resonance edge using circularly polarized light after cooling to 390 K, showing a clear SAXS ring with speckle. The shadow cast by the beamstop and some direct transmission though the pinhole and crossed TEM grids is visible in the centre of the image. The colour here represents the intensity of the difference image, with blue regions having a higher intensity of one polarization, whilst the red regions have a higher intensity from the other. (b) - (f) Example images where the temporal correlation analysis was performed taken at $t = 0$, 1310.4, 2620.8, 3931.2 and 5241.6 s. The speckle pattern clearly changes through the measurement time indicating the presence of dynamic behaviour. The black square in panel (a) marks the approximate position where these images were taken. (g) Example g_2 functions derived from the images (points) and the fits to equation 4 (lines) for various points on the cooling branch taken using circularly polarized light.

within the matrix of the other [35, 37]. In this scenario, there are two main sources of fluctuations: i) the nucleation or annihilation of regions of one phase within the other and ii) fluctuations in the region between the two phases [35, 37]. In FeRh, the inability to resolve all of the competing exchange interactions within the phase boundary wall would lead to magnetic frustration in this region meaning that fluctuations in the system would take place between spin configurations with degenerate energies [38, 39].

In the region around T_M when measured using XMCD, $\beta \sim 1$. At this stage of the transition, the FM regions will be separated by regions of AF material, meaning that long range interactions are unlikely to contribute to the dynamic behaviour. As the transition progresses and β increases towards 1.5, the FM domains get closer together, meaning that the long range interactions would begin to influence the magnetic structure both globally and within the phase boundary walls, leading to jammed dynamics.

For the measurements performed using XMLD, Fig. 3(c) shows that the behaviour is inherently different for $T > T_M$. In this region on both transition branches, the dynamic behaviour is diffusive with $\beta \sim 1$. The dynamic behaviour then becomes closer to $\beta \sim 1.5$ approaching T_M on both transition branches as seen by the inset in Fig. 3(c). Below T_M, β is mostly consistent with 1 within an error bar. The same behaviour is seen in reverse when heating.

The observation of $\beta \sim 1$ for the nominally fully AF and fully FM phases measured using XMLD, implies the presence of diffusive dynamic behaviour in these regions. The behaviour of the system measured using XMLD for the fully FM phase, where $T > T_M$, is in direct contrast to the jammed behaviour observed in the XMCD measurements. The opposite case is seen in the region close to $T = T_M$, where the XMLD exhibits jammed behaviour, whilst the XMCD measurements show diffusive behaviour.

This increase in β when heating past T_M for the XMLD measurements coincides with the introduction of FM material into the AF matrix when heating, and its removal when cooling. This change suggests that the properties of the system change fundamentally as FM material is introduced into the system. As this is a system in which AF regions are in direct contact with FM material, it suggests that the exchange coupling between the two magnetic phases plays a role in the dynamic behaviour of the system. The introduction of exchange coupling between the AF and FM regions would introduce an extra anisotropy energy into the system which would affect the behaviour of the spin-axes of both magnetic phases and the magnetic structure in the region between them. This would mean the phase boundary walls no longer operate as individual objects leading to collective dynamics, as consistent with the experimental data.

As the system jams approaching T_M when measured by XMLD it may be expected that the relaxation time, λ, would increase at this stage. The values of λ returned for the fits of Eq. 4 to the g_2 functions are shown as a function of temperature in Fig. 3(b) and (d) for the XMCD and XMLD experiments, respectively. λ is typically several hundred to one thousand seconds, but appears to peak around T_M for all measurement sets here. The presence of a peak implies that the freezing transition associated with a glass transition is not present

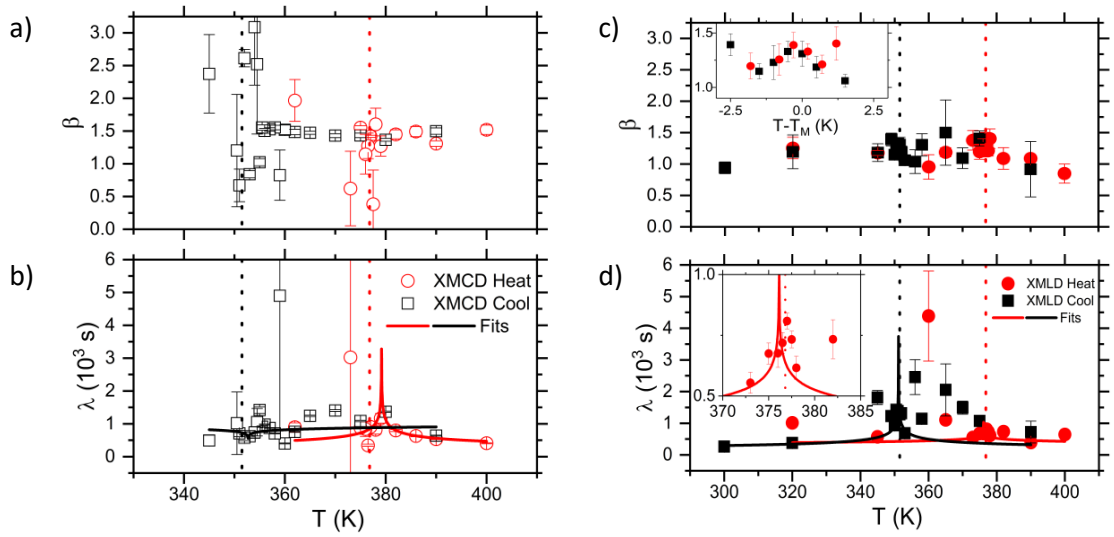

FIG. 3. Dynamic behaviour extracted from the XPCS measurement. Panels (a) and (b) show the behaviour of the stretching exponent, β, and the relaxation time, λ, extracted from the fits of equation 4 to the g_2 functions collected from XMCD measurements against temperature, T, through the transition. The inset in panel (c) shows the behaviour of β compared to the transition midpoint. Panels (c) and (d) shows the same quantity but for β and λ extracted from measurements performed using XMLD. The inset in panel (d) shows a close up of the behaviour of λ around the position of the transition midpoint. The black and red points are for measurements performed when cooling and heating, respectively. This convention is adopted for the remainder of this work and should be taken to be the case unless specified otherwise. There is a change in β approaching the transition midpoint measured by magnetometry, T_{M}, which is shown by the dashed lines. The direction of this change is dependent on the nature of the magnetic dichroism. The solid lines in panels (b) and (d) are fits of the critical slowing down model to the data, which shows good agreement with the behaviour seen.

[22, 26], nor can the behaviour be described well by the Arrhenius model [22, 37].

Another model often used to describe relaxation behaviour for systems undergoing a SOPT as it approaches the critical temperature associated with the transition, T_{c}, is that of critical slowing down [22, 40]. The dependence of the relaxation time, λ, upon its proximity to T_{c} is given by [22, 40]:

$$\lambda = \lambda_0 \left| 1 - \frac{T}{T_{\mathrm{C}}} \right|^{-zv}, \qquad (2)$$

where zv is the critical scaling exponent. The fitting of this equation to the data is shown by the solid lines in Fig. 3(c) and (d) for the XMCD and XMLD investigations, respectively. The inset in panel (d) shows a close up of the behaviour of the heating branch around T_{M} when measured using XMLD. The values returned from the fits for T_{c} are shown in the supplemental material. The values of zv extracted from these fits are shown in Fig. 5. The success of these fits implies that critical scaling of the relaxation time is observed approaching T_{M} through the FeRh metamagnetic phase transition when probed using XPCS. It is noted that critical slowing down is observed for all measurement sets except the measurements taken using XMCD when cooling, where no evidence of critical scaling with temperature is seen.

Critical scaling behaviour is typically associated with SOPTs where a divergence of the correlation length of thermal fluctuations is seen approaching T_{c} [40, 41]. The same behaviour is not expected through FOPTs [41], though critical scaling of the domain size of a given phase within the other has been seen through various FOPT systems [42], including FeRh [19]. However, in this experiment we are unable to reconcile the behaviour of the relaxation time with the measured length scale (see supplemental material). To try and isolate which relaxation pathway is responsible for this behaviour, a similar investigation of the relaxation behaviour was performed using magnetometry techniques. The results of this study are shown in Fig. 4.

The temporal evolution of the time dependent phase fraction, $\alpha(t)$ (see Methods for definition), is shown for various temperatures when heating in Fig. 4(a). α clearly varies through the measurement time, with the amplitude of this change peaking for measurements performed near T_{M}. By performing Avrami analysis (see Methods section) which is shown for the 376 K measurement in Fig. 4(b), it is clear that there are two regions where the expected linear dependence on $\ln(t)$ is observed. This indicates there are two relaxation processes occurring during the measurement time: i) the initial nucleation of FM domains due to thermal equalization of the system (henceforth labelled N) and ii) the subsequent growth (G) of these domains. The value of $\ln(K)$, where $K = \lambda^{-1}$

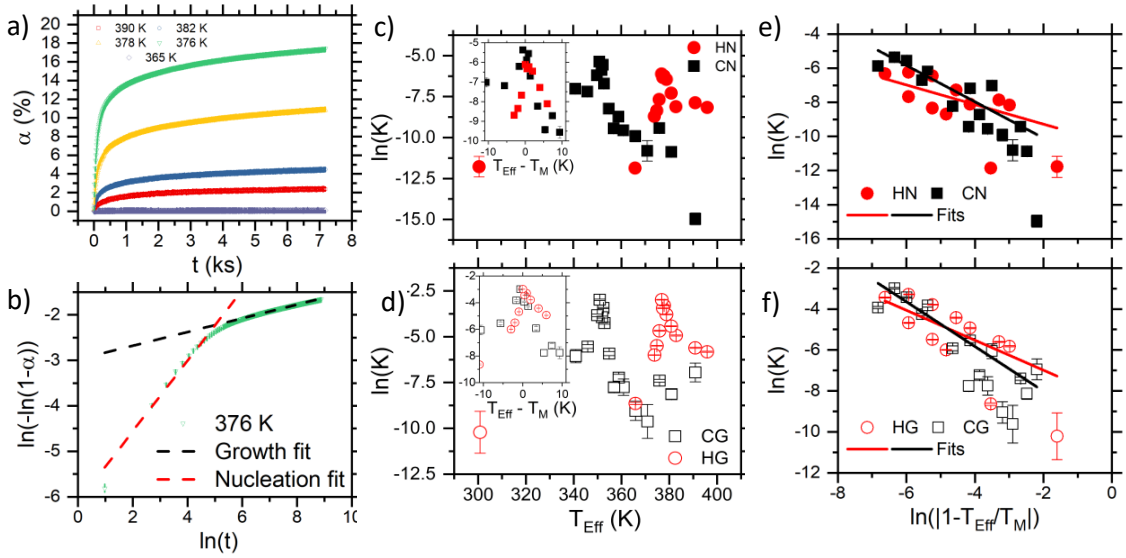

FIG. 4. Magnetic relaxation measured using magnetometry. (a) The evolution of α with time, t, for measurements performed at various temperatures when heating. (b) The Avrami analysis (see Methods section for description) for the measurement performed at 376 K. There are two regions where the linear relationship expected is observed here, which are believed to correspond to the nucleation (N) and subsequent growth (G) of domains in the system. The linear fits used to extract information from the two regions are shown by the dashed lines. Panels (c) and (d) show the value of $\ln(K)$ extracted from the Avrami analysis against the effective temperature, T_{Eff}, for the nucleation and growth phases respectively, for measurements performed when heating (H) and cooling (C). The insets in these figures show the behaviour of $\ln(K)$ against the deviation in temperature from the transition midpoint, $T_{\mathrm{Eff}} - T_{\mathrm{M}}$, zoomed in around $T_{\mathrm{Eff}} - T_{\mathrm{M}} = 0$. These figures demonstrate an increase in $\ln(K)$ approaching $T_{\mathrm{Eff}} - T_{\mathrm{M}} = 0$, which is indicative of critical speeding up. Panels (e) and (f) show the behaviour of $\ln(K)$ extracted for all measurements against the natural logarithm of the reduced temperature $1 - T_{\mathrm{Eff}}/T_{\mathrm{M}}$, for both the nucleation and growth phases respectively. The solid lines here are fits of the data to the critical slowing down model, the results of which are shown in Fig. 5. Critical speeding up is seen for all measurements sets here.

is the rate constant, extracted from Avrami analysis is shown against T_{Eff} for both the G and N regimes in Fig. 4(c) and (d), respectively. All measurements here show that $\ln(K)$ increases for $T_{\mathrm{Eff}} \sim T_{\mathrm{M}}$ as seen in the inset where the same data is plotted against $T_{\mathrm{Eff}} - T_{\mathrm{M}}$, which is indicative of critical speeding up. This is confirmed by plotting the behaviour of $\ln(K)$ in conjunction with the critical slowing down model described by Eq. 2 as seen in panels (e) and (f) of Fig.4. The lines here represent a fit to Eq. 2 where the value of T_{M} is assumed to be that extracted by magnetometry.

Fig. 5 shows a summary of the values of zv extracted for the fits of the critical slowing down model to the measurements performed using the various techniques, including through SOPT at the Curie temperature (see supplemental material). Here, $zv > 0$ indicates critical slowing down, whilst critical speeding up is present for $zv < 0$. Fig. 5 clearly demonstrates an asymmetry in the nature of the critical scaling for measurements performed using XPCS and magnetometry. The magnetometry measurements are expected to be more sensitive to the formation of domains than the fluctuations in the phase boundary walls, whereas the contrary is true for the XPCS measurements. From this evidence, the critical scaling of the domain formation and phase boundary wall fluctuations through the FOPT are different.

T_{M} is defined as the temperature where phase coexistence is maximised and where the difference in the free energy of the two states is minimised. The rate of domain nucleation would increase at this point, leading to the critical speeding up seen in the magnetometry measurements. For the same reason, the fluctuations within the phase boundary wall would also be expected to exhibit critical speeding up approaching T_{M}, where critical slowing down is instead seen. The XPCS measurements reveal that the introduction of exchange coupling has a profound effect on the dynamic behaviour of the system. The phase boundary wall in this material is seen to be an agglomeration of regions of the two magnetic orders formed by exchange coupling between the two phases [31]. The introduction of the exchange coupling, in combination with the minimization of the energy barrier between the two magnetic states, may blur the magnetic structure in the phase boundary wall increasing its effective dimensions approaching T_{M}. Such behaviour would mimic the divergence of the correlation length required for critical slowing down in SOPT systems, leading to the behaviour seen in the XPCS measurements and has

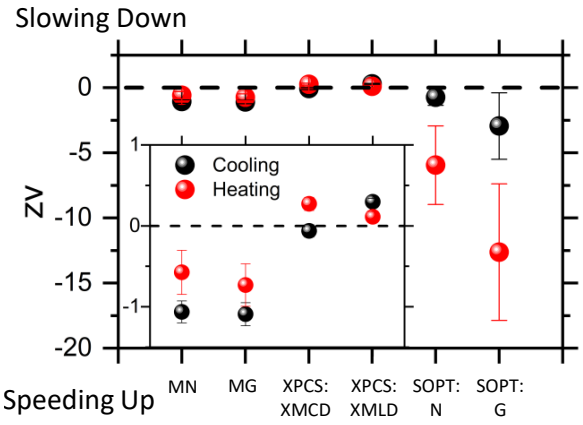

FIG. 5. Summary of critical scaling analysis. The value of the critical scaling exponent, zv, is shown for the various measurement techniques here for measurements performed both when heating and whilst cooling. Here, M means measurements performed using magnetometry through the first-order phase transition and SOPT refers to measurements performed using magnetometry through the second-order phase transition approaching the Curie temperature (see supplemental material). The definition of the critical slowing down model here means that $zv > 0$ is indicative of critical slowing down, whilst $zv < 0$ implies critical speeding up. There is a clear asymmetry between the measurements performed using magnetometry techniques and those performed using XPCS.

been observed in FOPT systems previously [43].

The demonstration of critical scaling behaviour emanating from the phase boundary wall is unexpected within the current framework of phase transition dynamics. It implies that latent heat, the defining feature of a FOPT [41], has little influence in the dynamic behaviour of the phase boundary wall. The interphase coupling however clearly plays a key role in determining the behaviour of the phase boundary wall. There are many ways that two states in a FOPT system can couple across the boundary including elastic coupling due to strain [7], magnetic coupling in metamagnetic transitions and charge coupling in metal-insulator systems [42, 43], which means that the influence of the interphase coupling upon the phase boundary wall dynamics should be considered as a fundamental property of FOPT systems. It also highlights the need for the consideration of coupled order parameters in theories of FOPT dynamics raised by Post *et al.* [43].

To conclude, XPCS investigations were performed using both XMCD and XMLD to measure the dynamic behaviour of the system through the FeRh metamagnetic FOPT. These investigations show a change in the nature of the dynamic behaviour centred on the transition midpoint. The direction in which this change takes place is different when measured with the two dichroism types. The jamming transition seen in the measurements performed using XMLD suggests that the introduction of exchange coupling has a profound effect on the dynamic behaviour of the system. Critical slowing down of the relaxation time is also observed in the XPCS measurements. To identify the source of this behaviour, measurements of the dynamic behaviour on the macroscale were performed using magnetometry techniques. These investigations reveal critical speeding up around the transition midpoint, which can be attributed to the reduction in the free energy difference between the two states at this point. The macroscale investigations imply that the behaviour measured using XPCS belongs to the phase boundary wall. The behaviour of the relaxation time extracted from the XPCS measurements then implies that the dimensions of the phase boundary wall scale critically with temperature approaching the transition midpoint. This can be attributed to the introduction of exchange coupling and the minimized free energy difference between the two magnetic phases at this temperature. The influence of interphase coupling on the behaviour of the phase boundary wall should be considered a fundamental property of first-order phase transitions.

METHODS

Growth and Characterization

The sample used in this experiment was a 100 nm thick FeRh layer grown on a 100 nm thick NiAl buffer layer deposited using DC magnetron sputtering on a molecular beam epitaxy-grown GaAs/AlAs/GaAs heterostructure substrate. The NiAl layer is also a B2-ordered material and improves the stability of the FeRh layer and promotes epitaxial growth [44]. The substrate was annealed overnight at 400°C, at which temperature the NiAl layer was deposited. The system was then heated to 600°C, where the FeRh layer was grown. The sample was then annealed *in situ* for 1 hour at 700°C. Structural characterization of the film was performed using x-ray diffraction (XRD). The magnetic properties of the sample were measured using a SQUID-vibrating sample magnetometer (SQUID-VSM) in a 1 T in-plane applied field.

Membrane Fabrication

The as-grown film was then made into a membrane suitable for x-ray transmission measurements using a HF etching process. This was performed following the method outlined in Ref. 45. The substrate was chosen for its known etching chemistry. By performing the etch in this manner, it is possible to destroy the AlAs layer without harming the rest of the sample. This creates a free standing FeRh/NiAl/GaAs layer, which was subsequently captured between two Cu TEM grids to provide an x-ray transparent sample of B2-ordered FeRh.

Soft X-Ray Methods

The RMSAXS and XPCS measurements were carried out at the I10 beamline of the Diamond Light Source. A 20 μm radius pinhole is placed in the beampath in front of the samples to provide the coherent light required to generate the speckle pattern [21, 22]. To increase the scattering from the magnetic parts of the sample, these measurements were performed with photon energies at the Fe L_3 resonance. This is measured to be between 706.4-707.2 eV at 400 K depending on the type of dichroism used. The images series were taken using a 2D charge coupled device (CCD) camera. For XPCS image series, in which consecutive images are performed with opposing helicities (XMCD) or polarization orientations (XMLD) and are combined in post-processing to increase the signal as per the method outlined by Fischer *et al.* [27]. In this protocol, the intensity of each image of the final image, I, is calculated using

$$I = I^{+} - I^{-}, \tag{3}$$

where I^{+} is the intensity of the image taken with a given helicity or linear polarization and I^{-} is the image taken using the opposite helicity or linear polarization. Each image series consists of 100 images calculated in this way and are taken over 90-120 minute periods, depending on the type of dichroism used. The sample was thermally cycled between each measurement to reset the domain structure. All measurements took place in the absence of a magnetic field.

For the RMSAXS, the first image of each series was taken and its radial average was calculated. This procedure was performed after any potential artifacts within the image, such as the grid, the back of the camera and any holes in the beamstop are removed. $Q = 0$ is taken to be the centre of mass of the image. The XPCS measurements of the dynamic behaviour were performed on a 200×200 pixel box centered around the peak in structural analysis (see supplemental material).

The temporal auto-correlations for each image series performed at a given temperature are calculated using a g_2 function. This function is calculated for a series of images separated by a time delay τ and takes the form [21–24, 26]

$$g_2(\tau) = \left\langle \frac{\langle I(\mathbf{Q},t) I(\mathbf{Q},t+\tau)\rangle_t}{\langle I(\mathbf{Q},t)\rangle_t^2} \right\rangle_{\mathbf{Q}} \tag{4}$$

where $I(\mathbf{Q},t)$ is the intensity at position $\mathbf{Q}$ at time t and where $\langle ... \rangle_{t,\mathbf{Q}}$ denotes an average over t or $\mathbf{Q}$. Here, the g_2 function is calculated for each individual pixel, which corresponds to a particular value of $\mathbf{Q}$, each of which is then averaged over the entire image to give the final g_2 function. τ is taken to be integer multiples of the time between images.

Magnetometry Measurements

The measurements of the magnetic relaxation performed were performed using the same SQUID-VSM in which the magnetization against temperature profiles shown in Fig. 1. For these measurements, for comparison with the XPCS investigations, the temperature was ramped at 2 K min^{-1} and the magnetization was measured for 2 hours immediately after the desired temperature was achieved. The sample was thermally cycled such that it entered the fully AF or FM state, depending on the temperature sweep direction, between measurements to reset the magnetic state.

The time dependent phase fraction, $\alpha(t)$, is defined as the ratio of the phase changed during the time interval, t, and the total available phase fraction available at that temperature and is calculated using[37]:

$$\alpha(t) = \frac{M(t) - M_{\mathrm{i}}}{M_{\mathrm{S}} - M_{\mathrm{i}}}, \tag{5}$$

where $M(t)$ is the magnetization at a given time, t, M_{i} is the magnetization at the beginning of the measurement time, M_{S} is either the saturation magnetization when heating, or the residual magnetization for measurements performed when cooling.

In the Avrami model, the time dependent phase fraction can be written in terms of an exponential probability distribution with a given rate, K, after a time t at a given temperature such that [37]:

$$\alpha(t) = 1 - e^{-Kt^n}, \tag{6}$$

where n is the Avrami exponent and refers to the dimensionality of the changes taking place within the system. It follows then that it is possible to extract both K and n using:

$$\ln(-\ln(1-\alpha)) = \ln(K) + n\ln(t). \tag{7}$$

It also follows from this equation that regions of the data where a straight line can be used to accurately describe the behaviour means that the system contains a single relaxation process with given dimensionality.

Measurements following the same protocol were also performed on a different FeRh sample, grown on MgO with the substrate still attached, through the second-order phase transition approaching the Curie temperature. See supplementary information for more details.

AUTHOR CONTRIBUTIONS

J.R.M. was responsible for the growth and characterization of the samples. J.R.M. and R.C.T. were responsible for the generation of the data analysis code, whilst J.R.M. performed the analysis. J.R.M. performed and analysed all of relaxation experiments performed in the magnetometer. N.A.P. is accredited with the fabrication

of the membrane samples and the HF etch. R.P.C. was responsible for the growth of the GaAs/AlAs/GaAs heterostructure substrate. R.F. and P.S. were local contacts at Diamond for the beamtime experiments. All authors bar N.A.P., R.C. and S.M. attended a beamtime experiment and were involved in the acquisition of the data. D.M, S.M., P.S. and C.H.M. supervised the project. All authors discussed and commented on the manuscript.

AUTHOR DECLARATIONS

The authors declare no competing financial interests.

ACKNOWLEDGMENTS

This work was supported by the Diamond Light Source and the UK EPSRC (grant numbers EP/M018504/1 and EP/M019020/1).

[1] Fallot, M. & Hocart, R. On the appearance of ferromagnetism upon elevation of the temperature of iron and rhodium. *Rev. Sci.* **8**, 498 (1939).

[2] Kouvel, J. S. & Hartelius, C. C. Anomalous magnetic moments and transformations in the ordered alloy FeRh. *J. Appl. Phys.* **33**, 1343 (1962).

[3] Kouvel, J. S. Unusual nature of the abrupt magnetic transition in FeRh and its pseudobinary variants. *J. Appl. Phys.* **37**, 1257 (1966).

[4] de Vries, M. A. *et al.* Hall-effect characterization of the metamagnetic transition in FeRh. *N. J. Phys.* **15**, 013008 (2013).

[5] Thiele, J. U., Maat, S. & Fullerton, E. E. FeRh/FePt exchange spring films for thermally assisted magnetic recording media. *Appl. Phys. Lett.* **82**, 2859 (2003).

[6] Cherifi, R. O. *et al.* Electric-field control of magnetic order above room temperature. *Nat. Mater.* **13**, 345 (2014).

[7] Lee, Y. *et al.* Large resistivity modulation in mixed-phase metallic systems. *Nat. Comms.* **6**, 5959 (2015).

[8] Marti, X. *et al.* Room-temperature antiferromagnetic memory resistor. *Nat. Mater.* **13**, 367 (2014).

[9] Le Graet, C. *et al.* Temperature controlled motion of an antiferromagnet- ferromagnet interface within a dopant-graded FeRh epilayer. *APL Materials* **3**, 041802 (2015).

[10] Moriyama, T. *et al.* Sequential write-read operations in FeRh antiferromagnetic memory. *Appl. Phys. Lett.* **107**, 122403 (2015).

[11] Temple, R. C. *et al.* Phase domain boundary motion and memristance in gradient-doped FeRh nanopillars induced by spin injection. *arXiv e-prints* arXiv:1905.03573 (2019).

[12] Maat, S., Thiele, J. U. & Fullerton, E. E. Temperature and field hysteresis of the antiferromagnetic-to-ferromagnetic phase transition in epitaxial FeRh films. *Phys. Rev. B* **72**, 214432 (2005).

[13] Baldasseroni, C. *et al.* Temperature-driven nucleation of ferromagnetic domains in FeRh thin films. *Appl. Phys. Lett.* **100**, 262401 (2012).

[14] Mariager, S. O., Le Guyader, L., Buzzi, M., Ingold, G. & Quitmann, C. Imaging the antiferromagnetic to ferromagnetic first order phase transition of FeRh. *arXiv e-prints* arXiv:1301.4164 (2013).

[15] Kinane, C. J. *et al.* Observation of a temperature dependent asymmetry in the domain structure of a Pd-doped FeRh epilayer. *N. J. Phys.* **16**, 113073 (2014).

[16] Baldasseroni, C. *et al.* Temperature-driven growth of antiferromagnetic domains in thin-film FeRh. *J. Phys. : Cond. Mater.* **27**, 256001 (2015).

[17] Almeida, T. P. *et al.* Quantitative TEM imaging of the magnetostructural and phase transitions in FeRh thin film systems. *Sci. Rep.* **7**, 17835 (2017).

[18] Gatel, C. *et al.* Inhomogeneous spatial distribution of the magnetic transition in an iron-rhodium thin film. *Nat. Comms.* **8**, 15703 (2017).

[19] Keavney, D. J. *et al.* Phase coexistence and kinetic arrest in the magnetostructural transition of the ordered alloy FeRh. *Sci. Rep.* **8**, 1778 (2018).

[20] Temple, R. C. *et al.* Antiferromagnetic-ferromagnetic phase domain development in nanopatterned FeRh islands. *Phys. Rev. Materials* **2**, 104406 (2018).

[21] Sinha, S. K., Jiang, Z. & Lurio, L. B. X-ray photon correlated spectroscopy studies of surfaces and thin films. *Advanced Materials* **26**, 7764 (2014).

[22] Morley, S. A. *et al.* Vogel-Fulcher-Tammann freezing of a thermally fluctuating artificial spin ice probed by x-ray photon correlation spectroscopy. *Phys. Rev. B* **95**, 104422 (2017).

[23] Chen, X. M. *et al.* Spontaneous magnetic superdomain wall fluctuations in an artificial antiferromagnet. *arXiv e-prints* 1809.05656 (2018).

[24] Shpyrko, O. G. *et al.* Direct measurement of antiferromagnetic domain fluctuations. *Nature* **447**, 68 (2007).

[25] Konings, S. *et al.* Magnetic domain fluctuations in an antiferromagnetic film observed with coherent resonant soft x-ray scattering. *Physical Review Letters* **106**, 077402 (2011).

[26] Chen, S.-W. *et al.* Jamming behavior of domains in a spiral antiferromagnetic system. *Phys. Rev. Lett.* **110**, 217201 (2013).

[27] Fischer, P., Zeller, R., Schütz, G., Georigk, G. & Haubold, H. Magnetic small angle x-ray scattering. *Journal de Physique IV* **7**, 753 (1997).

[28] Kortright, J. B. *et al.* Soft-x-ray small-angle scattering as a sensitive probe of magnetic and charge heterogeneity. *Phys. Rev. B* **64**, 092401 (2001).

[29] Bagschik, K. *et al.* Employing soft x-ray resonant magnetic scattering to study domain sizes and anisotropy in Co/Pd multilayers. *Phys. Rev. B* **94**, 134413 (2016).

[30] Stohr, J. & Siegmann, H. C. *Magnetism: From Fundamentals to Nanoscale Dynamics*, chap. 9 (Springer Series

in Solid State Physics, 2006).

[31] Massey, J. R. *et al.* Phase boundary exchange coupling in the mixed magnetic phase regime of a Pd-doped FeRh epilayer. *arXiv e-prints* arXiv:1807.01615 (2019).

[32] de Jeu, W. H., Madsen, A., Sikharulidze, I. & Sprunt, S. Heterodyne and homodyne detection in fluctuating smectic membranes by photon correlation spectroscopy at x-ray and visible wavelengths. *Physica B: Cond. Mat.* **357**, 39 (2005).

[33] Johnston, D. C. Stretched exponential relaxation arising from a continuous sum of exponential decays. *Phys. Rev. B* **74**, 184430 (2006).

[34] Hansen, E. W., Gong, X. & Chen, Q. Compressed exponential response function arising from a continuous distribution of gaussian decays - distribution characteristics. *Macro. Chem. and Phys.* **214**, 844 (2013).

[35] Binder, K. Theory of first-order phase transitions. *Reports on Progress in Physics* **50**, 783 (1987).

[36] Banigan, E. J., Illich, M. K., Stace-Naughton, D. J. & Egolf, D. A. The chaotic dynamics of jamming. *Nature Physics* **9**, 288 (2013).

[37] Loving, M. *Understanding the Magnetostructural Transformation in FeRh thin films.* Ph.D. thesis, The Department of Chemical Engineering, Northeastern University (2013).

[38] Ostler, T. A., Barton, C., Thomson, T. & Hrkac, G. Modeling the thickness dependence of the magnetic phase transition temperature in thin FeRh films. *Phys. Rev. B* **95**, 064415 (2017).

[39] Blundell, S. *Magnetism In Condensed Matter*, chap. 8, 166 (Oxford University Press, 2001).

[40] Djurberg, C. *et al.* Dynamics of an interacting particle system: Evidence of critical slowing down. *Phys. Rev. Lett.* **79**, 5154 (1997).

[41] Porter, D. A. & Easterling, K. E. *Phase Transformations in Metals and Alloys*, chap. 5 (Van Nostrand Reinhold Publishing, 1981).

[42] McLeod, A. S. *et al.* Nanotextured phase coexistence in the correlated insulator V_2O_3. *Nat. Physics.* **13**, 80 (2016).

[43] Post, K. W. *et al.* Coexisting first- and second-order electronic phase transitions in a correlated oxide. *Nat. Physics.* **14**, 1056 (2018).

[44] Kande, D., Pisana, S., Weller, D., Laughlin, D. E. & Zhu, J. G. Enhanced B2 ordering of FeRh thin films using B2 NiAl underlayers. *IEEE Transactions on Magnetics* **47**, 3296 (2011).

[45] Russell, C. *et al.* Spectroscopy of polycrystalline materials using thinned-substrate planar goubau line at cryogenic temperatures. *Lab on a Chip* **13**, 4065 (2013).

Second-Order Phase Transition At The Phase Boundary Through The FeRh First-Order Metamagnetic Phase Transition: Supplementary Information

Jamie R. Massey,[1,*] Rowan C. Temple,[1] Trevor P. Almeida,[2] Ray Lamb,[2] Nicolas A. Peters,[1,3] Richard P. Campion,[4] Raymond Fan,[5] Damien McGrouther,[2] Stephen McVitie,[2] Paul Steadman,[5] and Christopher H. Marrows[1,†]

[1]*School of Physics and Astronomy, University of Leeds, Leeds LS2 9JT, United Kingdom.*

[2]*SUPA, School of Physics and Astronomy, University of Glasgow, Glasgow, G12 8QQ, United Kingdom.*

[3]*School of Electronic and Electrical Engineering, University of Leeds, Leeds, LS2 9JT, United Kingdom.*

[4]*School of Physics and Astronomy, University of Nottingham, Nottingham, NG7 2RD, United Kingdom.*

[5]*Diamond Light Source, Chilton, Didcot, OX11 0DE, United Kingdom.*

(Dated: December 19, 2019)

* J.R.Massey@leeds.ac.uk

† c.h.marrows@leeds.ac.uk

EFFECTIVE TEMPERATURE

The transition temperature, T_{T}, of the metamagnetic phase transition in FeRh is sensitive to the application of external magnetic field, H_{Ext} [1, 2]. As such, when comparing between measurement performed whilst a magnetic field is applied to those performed in the absence of an external magnetic field, it is necessary to correct the temperature of the measurements in which a field is applied. This corrected temperature is known as the effective temperature, T_{Eff}, and is defined as the temperature at which the same magnetization is expected in the absence of external field [2]. The formula used for its calculation is given by,

$$T_{\mathrm{Eff}} = T_0 - \frac{dT_{\mathrm{T}}}{d(\mu_0 H_{\mathrm{Ext}})}\mu_0 H_{\mathrm{Ext}}, \tag{1}$$

where T_0 is the real sample temperature, μ_0 is the permeability of free space and $dT_{\mathrm{T}}/d(\mu_0 H_{\mathrm{Ext}}$ is the rate of change of the T_{T} with $\mu_0 H_{\mathrm{Ext}}$.

The dependence of the transition upon varying magnetic field values can be seen by the points in Fig. 1(a). This figure shows the temperature derivative of the magnetization dM/dT for a series of field values, where the position of the peak in dM/dT clearly decreases in temperature with increasing field. The value of T_{T} is extracted by fitting a Gaussian curve to dM/dT [1], which can be seen by the dashed and solid lines in this figure for measurements performed when cooling and heating, respectively. The extracted values of T_{T} are shown against their respective value of $\mu_0 H_{\mathrm{Ext}}$ for both the heating and cooling branches in Fig. 1. The linear fit here is used to extract $dT_{\mathrm{T}}/d(\mu_0 H_{\mathrm{Ext}})$ and also the transition midpoint at zero field, T_{M}, as the absiccsa intercept. Values extracted for these measurements are shown in Table I.

TABLE I. Results of linear fits to the dependence on T_{T} on $\mu_0 H_{\mathrm{Ext}}$.

	$\frac{dT_{\mathrm{T}}}{d(\mu_0 H_{\mathrm{Ext}})}$ (K T^{-1})	T_{M} (K)
Heating	$-(7.99 \pm 0.02)$	376.85 ± 0.02
Cooling	$-(8.76 \pm 0.03)$	351.47 ± 0.03

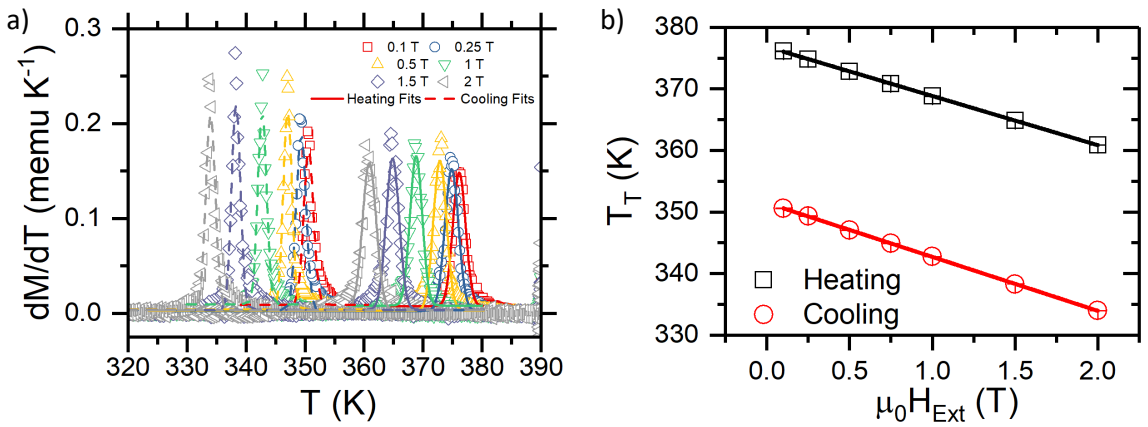

FIG. 1. Dependence of the transition temperature, T_{T}, in response to external magnetic field. Panel (a) shows the dependence of the temperature, T, derivative of the magnetization, dM/dT, against T for measurements performed in various external magnetic field strengths (points). The solid and dashed lines in this figure are Gaussian fits to the data performed when heating and cooling respectively. Panel (b) shows the value of the extracted values of T_{T} against the external magnetic field in which the measurements was performed. The linear fit here is used to extract $dT_{\mathrm{T}}/d(\mu_0 H_{\mathrm{Ext}})$ and the transition midpoint at zero field, T_{M}.

DEMONSTRATION OF RESONANT MAGNETIC SAXS

Evidence for the presence of RMSAXS can be seen in panels (a)-(d) of Fig. 2. These images are examples of those taken with the beam energy both off (panels (a) and (c)) and on (panels (b) and (d)) the Fe L_3 resonance for images taken using circularly (panels (a) and (b)) and linearly (panels (c) and (d)) polarized light. These images are taken using the protocol outlined in the methods section of the main document. Both images taken with beam energies away from the Fe L_3 edge show no appreciable scattering of any kind, whilst those taken on the Fe L_3 edge clearly show a SAXS ring with speckle features. The resonant enhancement of the scattering proves that it originates from magnetic order within the sample. The presence of speckle indicates the presence of a disordered magnetic structure, which is consistent with the expected magnetic domain structure at this point in the transition [3, 4].

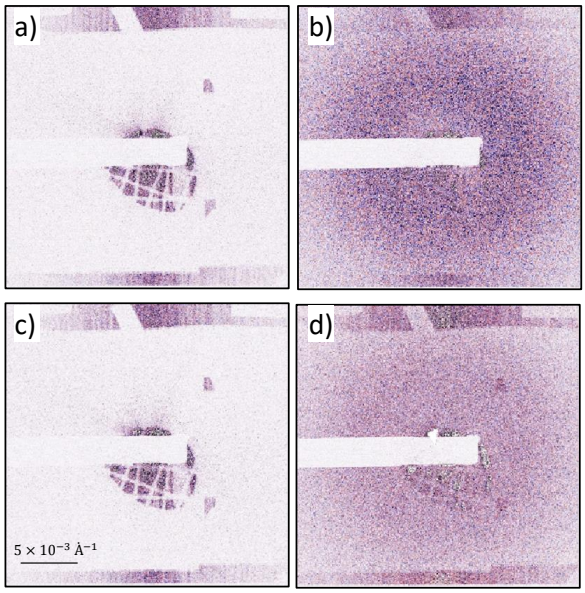

FIG. 2. Transmission RMSAXS patterns. (a) Image taken with a beam energy of 690 eV–off-resonance–at 400 K using circularly polarized light, showing no appreciable scattering. (b) Image taken on the Fe L_3 resonance edge using circularly polarized light, showing a clear SAXS ring with speckle. Equivalent images for linearly polarized light are shown in panels (c) and (d). In all four images the shadow cast by the beamstop is visible as a white rectangle on the left, and the pinhole and crossed TEM grids are visible in the centre of each image.

RESONANT MAGNETIC SAXS: STRUCTURAL ANALYSIS

To analyse the RMSAXS rings, we calculated the radial average of the intensity profile $I(Q)$ for the first image of each of the XPCS sets, where Q is the wavevector transfer. Examples of these for linearly polarised light can be seen in Fig. 3. This reveals a peak which corresponds to correlations in the structure factor [5, 6]. These are presented in normalised form as $I_{\mathrm{Norm}}(Q) = (I(Q) - I_{\mathrm{Min}})/(I_{\mathrm{Max}} - I_{\mathrm{Min}})$. A log-normal distribution was fitted to each data set to identify the position of the peak [7], $Q_{\mathrm{Peak}} = Q_0 e^{-\omega^2}$, where Q_0 is the centre of the distribution and ω is the logarithm of the full width at half maximum (FHWM) of the peak. It is then possible to extract the spatial lengthscale associated with the peak, $d = 2\pi/Q_{\mathrm{Peak}}$, the results of these fittings for all measurements taken using both circular and linear polarisation are shown in Fig. 4.

Fig. 4(a) shows measurements taken using circular light for both heating and cooling

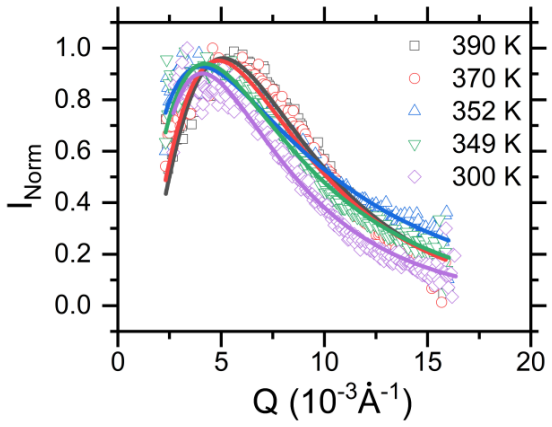

FIG. 3. Examples of the radial intensity profiles (points) and the fit of a log-normal distribution to the data (lines) taken at various temperatures on the cooling branch using linearly polarized light.

branches. These reveal an increase towards a peak value at $d \sim 400$ nm when heating, which occurs at around 377 K. The dashed lines here mark the position of the transition midpoint, T_{M}, calculated as the steepest point in the magnetometry trace in Fig. 4(e). At temperatures in excess of T_{M}, d is seen to decrease again, falling to 150 nm at 400 K. A similar behaviour is seen when cooling, though d is seen to be constant at around 150 nm until the temperature falls below 350 K, after which it is seen to increase, also to about 300 nm, before just starting to drop. These measurements performed during cooling also see the peak value occurring for $T = T_{\mathrm{M}}$. In order to understand these findings it is necessary to consider the development of the magnetic domain structure through the transition.

Previous real-space imaging has shown that FM domains in FeRh nucleate as flux closed structures around 200 nm in diameter on heating out of the fully AF phase [3, 4]. As the transition progresses, these domains begin to agglomerate, surrounding small residual patches of AF material before the film becomes fully FM with the domain structure taking up a striped configuration in the absence of a magnetic field, where the stripes have μm dimensions [3, 4]. Scattering from objects of this size would fall outside the available Q range, however scattering across the domain wall between the domains may be accessible. In this system, there are two types of domain wall scattering to consider: i) that between adjacent FM domains and ii) those between domains that are separated by regions of AF material. The lengthscale associated with scattering from these two objects would have different temperature dependences through the transition. Given the limited Q range and

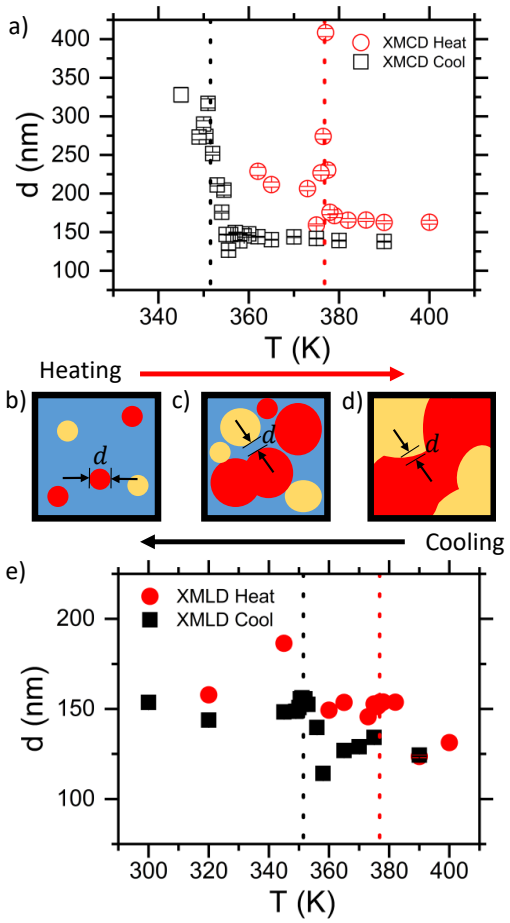

FIG. 4. Radial analysis results. (a) and (e) show the length d that corresponds to the position of the peaks seen in the radial intensity profiles, Q_{Peak}, against T for measurements performed using circularly (labelled XMCD) and linearly (labelled XMLD) polarized light respectively. The dashed lines in these panels show the position of the transition midpoint, T_{M}, for each branch, extracted from the magnetometry. Note the different T scales on the abscissae of the two graphs. Panels (b) - (d) show cartoons of the magnetic state at various points through the transition. In these diagrams, the blue depicts AF material and the red and yellow regions are FM domains with the magnetization oriented in opposite directions. The arrows are used to demonstrate the temperature sweep direction.

the changing nature of the domain structure in this experiment, it may be expected that the nature of the scatter changes across the transition.

To help aid the discussion, diagrams of the magnetic states through the transition are included in panels (b)-(d) in Fig. 4. The blue regions depict regions of AF material, whilst

the red and yellow regions are FM domains with their magnetization aligned in opposite directions. The black bars are used to demonstrate the source of the scattering object at each stage.

Considering the measurements performed using circular light in Fig. 4(a), when $T < T_{\mathrm{M}}$, the measured size of the scattering object d is consistent with the size of the FM domains seen in these previous works [3, 4, 8]. It is therefore reasonable to think that the scattering objects are the FM domains that have nucleated from the AF phase as the transition begins, which is shown by Fig. 4(b). On heating, it is known that the size of the domains would increase, which is reasonable up to T_{M} but is contradictory to the behaviour seen here at higher temperatures. Nevertheless, is also known that there will still be regions of AF material present between these domains they aggolomerate [3, 4, 8–10], which will shrink when approaching the fully FM phase, decreasing the distance between FM domains. These gaps between the FM phase regions now become the scattering objects, as shown in Fig. 4(c). When cooling from high temperatures, d is invariant down to about 360 K. These temperatures are consistent with the fully FM phase when measured using magnetometry and so the scattering in this regime is believed to correspond to domain walls between FM regions with different magnetization directions, as seen in Fig. 4(d). Approaching the transition, the rise and fall in d as it passed through a peak at T_{M} corresponds to the processes on the heating branch in reverse.

Turning to the measurements using linear light in Fig. 4(e), the overall behaviour is consistent, with peaks in d appearing at T_{M} on each branch, although it is less pronounced on the cooling branch. The length scales extracted for $T > T_{\mathrm{M}}$ appear to be consistent with the corresponding points measured using circular light. Therefore, the nature of the scatterers in this region is believed to be the same in both measurements. However, the behaviour of the two diverges for $T < T_{\mathrm{M}}$, where the measurements taken using linearly polarized light appear to be constant at $d \approx 150$ nm down to temperatures of 300 K for both transition branches. This behaviour is consistent with that seen in the only other previous magnetic imaging experiments on the AF phase of FeRh [11] and hence this behaviour is attributed to a change in scatterer at T_{M}. At 300 K, the system would exhibit only a 4 % FM volume fraction. Therefore as XMLD is sensitive to the presence of AF materials, the change in scatterer at this stage is believed to be AF domain structures, mirroring the FM domain structures causing scattering at the highest temperatures for the circular light

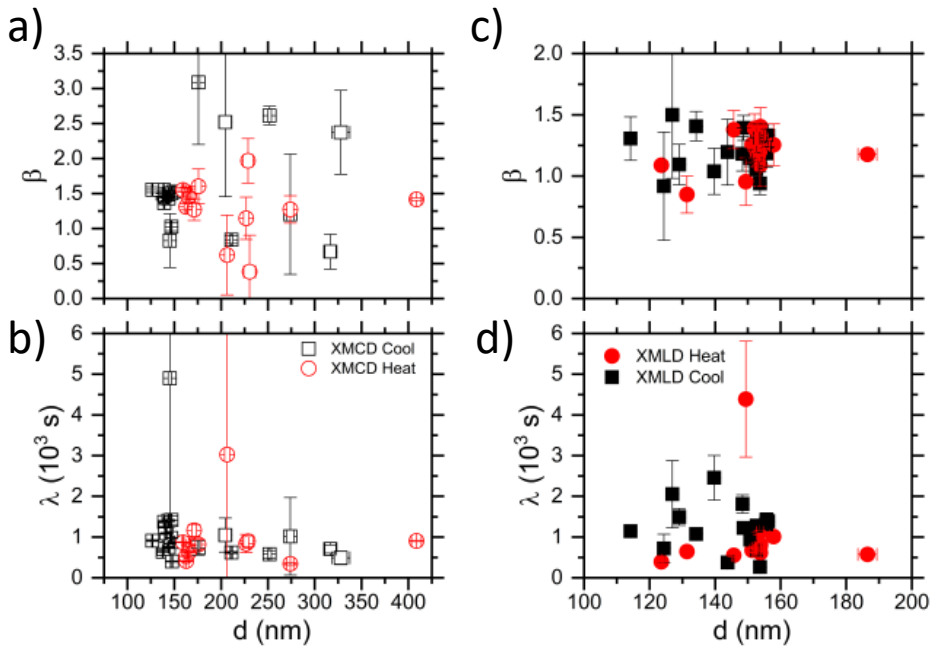

FIG. 5. Dependence of the dynamic behaviour on extracted lengthscale. Panels (a) and (b) show dependence of the values of the stretching exponent, β, and the relaxation time, λ, extracted from the analysis of the temporal correlation functions against the extracted length scale, d, for the measurements performed using XMCD. Panels (c) and (d) shows the same analysis for the measurements performed using XMLD. There is no clear correlation between either β or λ on d for any of the measurement sets here.

measurements. This demonstrates that it is possible to directly measure AF materials using RMSAXS and linearly polarised light.

DEPENDENCE OF THE DYNAMIC BEHAVIOUR ON THE EXTRACTED LENGTH-SCALE

As explained in the main body of this work, the dynamic behaviour of the system can sometimes be reliant upon the length scales present in the system [12–14], particularly in the case of critical scaling. The values of the stretching exponent, β, and the relaxation time, λ, extracted from the analysis of the temporal correlation functions are shown in Fig. 5 against the extracted length scale, d, for all measurements. Measurements performed using

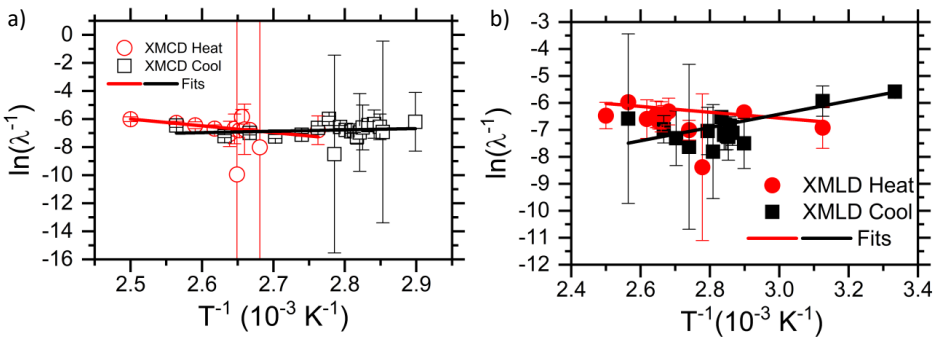

FIG. 6. Arrhenius analysis for the XPCS measurements. Panel (a) shows the behaviour of the relaxation time, λ extracted from the fits of the g_2 equation to the XPCS data for measurements performed using XMCD when both heating and cooling. Panel (b) shows the same information for measurements performed using XMLD. The solid lines here are fits to Eq. 2. The Arrhenius model is found to describe the behaviour of the heating branch measurements well, but leads to a negative activation energy for measurements performed when cooling, which is a non-physical result.

XMCD are shown in panels (a) and (b), whilst measurements performed using XMLD are shown in panels (c) and (d). It is clear from this figure that there is no real correlation or dependence of either of the quantities governing the dynamic behaviour upon d. Therefore, we are unable to reconcile the changes in the dynamic behaviour seen in this work with the changes in the nature of the scatterer through the transition.

ARRHENIUS ANALYSIS OF XPCS MEASUREMENTS

The Arrhenius model is used to describe systems where a relaxation process is governed by a temperature independent activation energy, E_{A} [12]. The relationship between the relaxation rate λ^{-1}, where λ is the relaxation time, and the temperature, T, is given by:

$$\ln(\lambda^{-1}) = \ln(\lambda_0^{-1}) - \frac{E_{\mathrm{A}}}{k_{\mathrm{B}}T}, \tag{2}$$

where λ_0^{-1} is the relaxation time at $T = 0$ and k_{B} is the Boltzmann constant [15]. Arrhenius analysis was performed on the XPCS measurements and the results are shown in Fig. 6 for measurements performed using both XMCD (panel (a)) and the XMLD (panel (b)).

The solid lines in Fig. 6 are fits of Eq. 2 to the behaviour of the relaxation time extracted

from the XPCS measurements. This model is found to describe well the behaviour of the measurements performed when heating, yielding $E_A/k_B = 4800 \pm 600$ K and $E_A/k_B = 1100 \pm 500$ K for the XMCD and XMLD measurements respectively. The difference here suggests an asymmetry in the nature of the behaviour probed, consistent with the difference in the nature of the probe itself. This model yields a negative activation energy for both data sets taken when cooling. This is a non-physical result and implies this model cannot adequately describe the behaviour seen in those datasets.

MAGNETIC VISCOSITY MEASURED USING A MAGNETOMETER UNDER VARYING CONDITIONS

The results of the magnetic viscosity measurements performed using a magnetometer presented in the main body of the text are those that best replicate the conditions used in the XPCS experiment with regards to the temperature sweep rate. In these measurements a field is required to prevent artefacts being introduced into the data. Also performed were measurements of the same sample that use a temperature sweep rate of 10 K min^{-1} with no external magnetic field applied. These are found to have two regimes of development as consistent with those presented in the main body of the text. After being analysed in the same way as those in the main document, the extracted values of $\ln(K)$ are plotted against $\ln|1 - T_{Eff}/T_M|$ in Fig. 7 for measurements performed whilst both heating (panel (a)) and cooling (panel (b)). In conjunction with the critical slowing down model presented in the main text, a linear fit is applied to extract the critical scaling exponent, zv, for each data set, the results of which are presented in Table II. Critical speeding up is observed for all data sets here.

EXTRACTED VALUE OF THE CRITICAL TEMPERATURE FROM THE XPCS DATA

The values of the critical temperature, T_c, associated with the critical slowing down seen in the XPCS measurements are shown in Table III. All of these values are consistent with T_M extracted from the magnetometry measurements within 2-3 error bars.

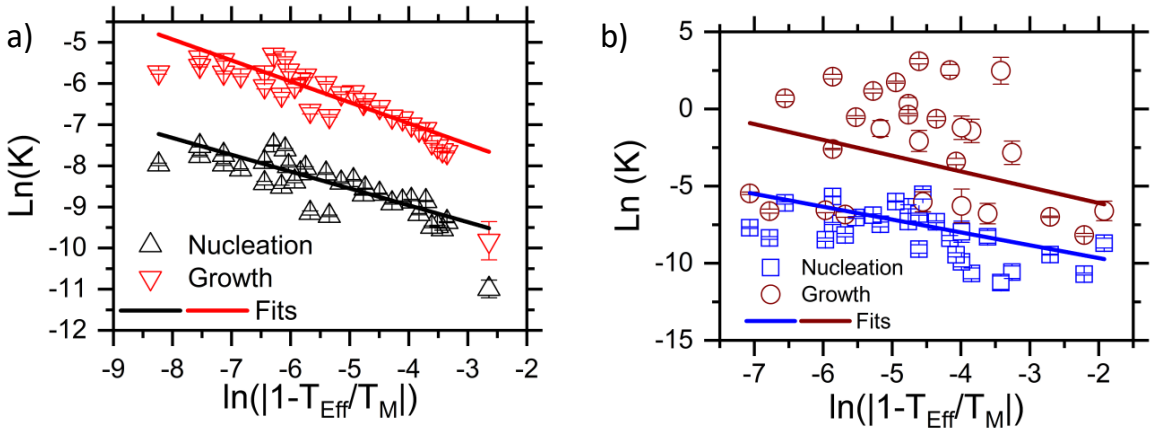

FIG. 7. Results of Avrami analysis for magnetometer based magnetic viscosity measurements performed under varying conditions. Panel (a) shows the values of $\ln(K)$ extracted for fits to measurements performed when heating, for both the nucleation and growth regimes, plotted against $\ln|1 - T_{\rm Eff}/T_{\rm M}|$. Panel (b) shows the same quantities extracted from the fits to measurements performed when cooling. The solid lines in these figures show linear fits in conjunction with the critical slowing down model presented in the main text. All data sets here present evidence of critical speeding up.

BEHAVIOUR OF THE AVRAMI EXPONENT

The Avrami analysis shown in the main body of the text contains a constant, n, which is known as the Avrami constant [15]. The extracted value of n for both the nucleation (N) and growth (G) phases of the dynamic behaviour is shown for all measurements presented in the main body of the text in Fig. 8(a) and (b) respectively. The extracted values of n

TABLE II. Results of critical scaling exponent, zv, extracted by fitting of the critical slowing down model to the magnetometer based magnetic viscosity measurements taken in the absence of magnetic field.

	Nucleation	Growth
Heating	$-(0.41 \pm 0.04)$	$-(0.51 \pm 0.04)$
Cooling	$-(0.8 \pm 0.1)$	$-(1 \pm 0.4)$

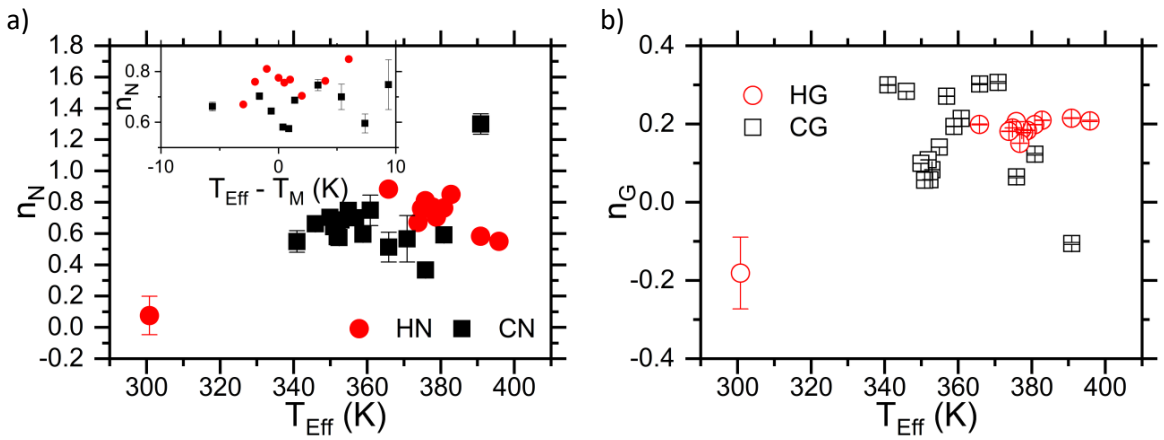

FIG. 8. Behaviour of the Avrami exponent through the transition. Panel (a) shows the behaviour of the Avrami exponent, n, extracted for the measurements performed using a magnetometer presented in the main body of the work for the nucleation (N) regime. The inset in panel (a) shows the behaviour of n centered around the transition midpoint, T_{M}. Panel (b) shows the same quantities but extracted from the fits to the growth regime. Red points show measurements performed when heating whilst black points are used to show measurements when cooling. All measurement sets here see a variation in the extracted value of n for $T_{\mathrm{Eff}} \sim T_{\mathrm{M}}$ except the behaviour of the growth phase when heating.

are typically between 0 and 1 and appear to vary again around the transition midpoint, for all measurement sets apart from the growth phase when heating. The cooling branch measurements see the value of n decrease for $T \sim T_{\mathrm{M}}$ for both types of phase kinetics here, whilst the heating branch measurements see an increase for the nucleation phase, but no change for the growth phase.

TABLE III. Results of critical temperature, T_c, extracted by fitting of the critical slowing down model to the relaxation time extracted from the XPCS measurements. All values are presented in K.

	XMCD	XMLD
Heating	379 ± 1	376 ± 1
Cooling	353 ± 5	351.2 ± 0.2

The Avrami exponent is linked to the number of dimensions in which the changes within the sample take place [15, 16]. Avrami exponents of less than 1 have been attributed to the influence of more than characteristic relaxation time for a given kinetic process [16]. The change in the value of n approaching T_{M} then implies that the number of relaxation times changes at this temperature. This is likely to be due to the reduction in the relative energy barrier approaching this temperature and the distribution of transition temperatures through the film giving rise to a number of different environments each with their own kinetic properties.

DYNAMIC INVESTIGATIONS THROUGH THE SECOND-ORDER FERROMAGNET TO PARAMAGNET PHASE TRANSITION AT THE CURIE TEMPERATURE

Further to the investigations focused on the behaviour of the system in proximity to the first-order transition (FOPT) temperature presented in the main body of this work, similar investigations were also performed through the second-order phase transition (SOPT) taking place at the Curie temperature, T_{C}. These were performed in the magnetometer in an externally applied field of 0.1 T. Due to the fragility of the sample used in the XPCS experiments these investigations are performed on a different 60 nm thick FeRh sample which is grown on MgO. The temperature dependent magnetization profile of the sample taken between 300-700 K is shown in Fig. 9(a) and shows a FOPT between 300-450 K, as well as a SOPT around 670 K. To identify the exact position of T_{C}, the data between 450 and 700 K is fitted to the following equation [17],

$$M = M_0\left(1 - \frac{T}{T_{\mathrm{C}}}\right)^{\beta}, \tag{3}$$

where M_0 is the magnetization at 0 K and β denotes the nature of the approach towards the SOPT. The fits here yield values of $\beta = 0.493 \pm 0.001$ and $\beta = 0.467 \pm 0.001$ for fits to the heating and cooling branches respectively, which gives reasonable agreement with the mean-field model as consistent with previous measurements [2]. The values of $T_{\mathrm{C}} = 669.6 \pm 0.1K$ and $T_{\mathrm{C}} = 671.8 \pm 0.1$ K were extracted for the heating and cooling branches respectively.

Again, performing the Avrami analysis on this system reveals two distinct regions where a linear relationship between $\ln(-\ln(1-\alpha))$ is observed as seen for the measurements per-

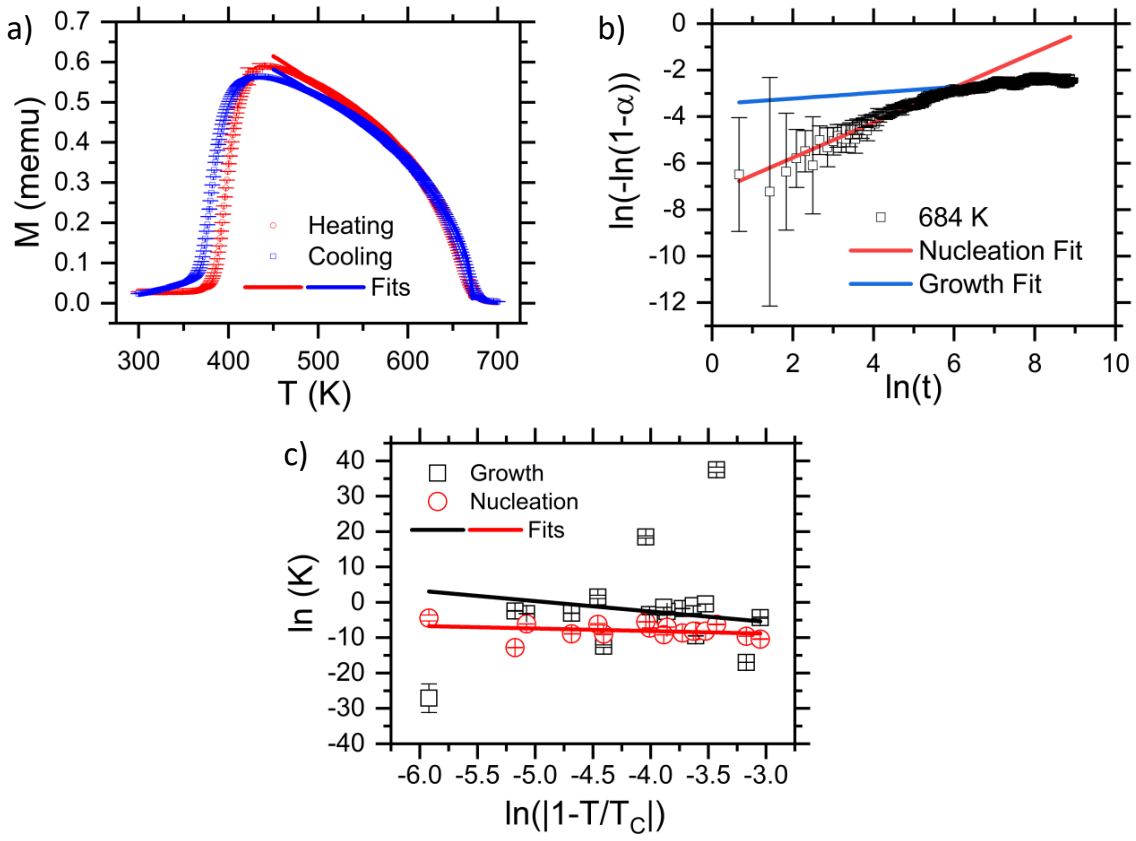

FIG. 9. Magnetometry based magnetic viscosity measurements through the second-order phase transition at the Curie temperature, T_{C}. Panel (a) shows the magnetization against temperature profile of a 60 nm FeRh sample grown on MgO between 300 - 700 K performed in a 0.1 T externally applied magnetic field. The blue points are those taken whilst cooling, and the red points are those taken when heating. Panel (b) shows examples of the Avrami analysis for a measurements performed at 684 K after cooling from 720 K. The solid lines show the fits for the two distinct regions of dynamic behaviour. Panel (c) shows the extracted values of $\ln(K)$ from the Avrami analysis plotted against $\ln|1 - T/T_{\mathrm{C}}|$ for measurements performed when cooling through the second-order phase transition at T_{C}. A weak dependence on the proximity to the phase transition is seen here.

formed at 684 K in Fig. 9(b), which is again attributed to the nucleation and growth of domains. The fits to the data for the two regions are shown by the solid lines in this figure. Fig. 9(c) shows the behaviour of $\ln(K)$ extracted from the Avrami analysis for the measurements performed when cooling through the SOPT against $\ln|1 - T/T_{\mathrm{C}}|$. Here, as all of the measurements are performed in the same applied field there is no need to correct the temperature. A weak dependence on the rate constant upon the proximity to T_{C} is seen

here, with the values extracted when both heating and cooling towards the SOPT shown in the summary of extracted values of zv in the main text. Only one of the measurements (growth phase for heating) demonstrates a value of zv that is significantly different from 0 within a 95% confidence level.

---

[1] Maat, S., Thiele, J. U. & Fullerton, E. E. Temperature and field hysteresis of the antiferromagnetic-to-ferromagnetic phase transition in epitaxial FeRh films. *Phys. Rev. B* **72**, 214432 (2005).

[2] Massey, J. R. *et al.* Phase boundary exchange coupling in the mixed magnetic phase regime of a Pd-doped FeRh epilayer. *arXiv e-prints* arXiv:1807.01615 (2019).

[3] Almeida, T. P. *et al.* Quantitative TEM imaging of the magnetostructural and phase transitions in FeRh thin film systems. *Sci. Rep.* **7**, 17835 (2017).

[4] Temple, R. C. *et al.* Antiferromagnetic-ferromagnetic phase domain development in nanopatterned FeRh islands. *Phys. Rev. Materials* **2**, 104406 (2018).

[5] Sivia, D. S. *Elementary Scattering Theory For X-Ray and Neutron Users*, chap. 5 (Oxford University Press, 2011).

[6] Bagschik, K. *et al.* Employing soft x-ray resonant magnetic scattering to study domain sizes and anisotropy in Co/Pd multilayers. *Phys. Rev. B* **94**, 134413 (2016).

[7] Fischer, P., Zeller, R., Schütz, G., Georigk, G. & Haubold, H. Magnetic small angle x-ray scattering. *Journal de Physique IV* **7**, 753 (1997).

[8] Baldasseroni, C. *et al.* Temperature-driven nucleation of ferromagnetic domains in FeRh thin films. *Appl. Phys. Lett.* **100**, 262401 (2012).

[9] Kinane, C. J. *et al.* Observation of a temperature dependent asymmetry in the domain structure of a Pd-doped FeRh epilayer. *N. J. Phys.* **16**, 113073 (2014).

[10] Mariager, S. O., Le Guyader, L., Buzzi, M., Ingold, G. & Quitmann, C. Imaging the antiferromagnetic to ferromagnetic first order phase transition of FeRh. *arXiv e-prints* arXiv:1301.4164 (2013).

[11] Baldasseroni, C. *et al.* Temperature-driven growth of antiferromagnetic domains in thin-film FeRh. *J. Phys. : Cond. Mater.* **27**, 256001 (2015).

[12] Chen, S.-W. *et al.* Jamming behavior of domains in a spiral antiferromagnetic system. *Phys.*

Rev. Lett. **110**, 217201 (2013).

[13] Djurberg, C. *et al.* Dynamics of an interacting particle system: Evidence of critical slowing down. *Phys. Rev. Lett.* **79**, 5154 (1997).

[14] Morley, S. A. *et al.* Vogel-Fulcher-Tammann freezing of a thermally fluctuating artificial spin ice probed by x-ray photon correlation spectroscopy. *Phys. Rev. B* **95**, 104422 (2017).

[15] Loving, M. *Understanding the Magnetostructural Transformation in FeRh thin films.* Ph.D. thesis, The Department of Chemical Engineering, Northeastern University (2013).

[16] Lin, F. X., Zhang, Y. B., Tao, N., Pantleon, W. & Jensen, D. J. Effects of heterogeneity on recrystallization kinetics of nanocrystalline copper prepared by dynamic plastic deformation. *Acta Materialia* **72**, 252 (2014).

[17] Blundell, S. *Magnetism in Condensed Matter*, chap. 6 (Oxford University Press, 2001).